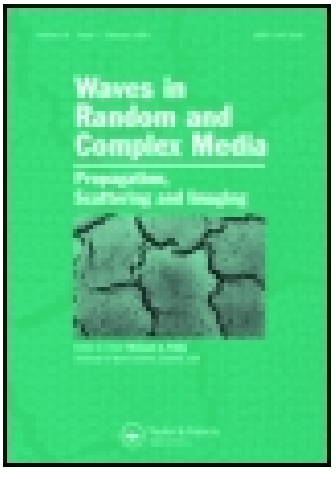

Waves in Random and Complex Media
Publication details, including instructions for authors and subscription information:
http://www.tandfonline.com/loi/twrm20

A short remark on the band structure of free-edge platonic crystals

Michael J.A. Smith[a], Michael H. Meylan[b], Ross C. McPhedran[c] & Chris G. Poulton[d]

[a] Institut Fresnel, UMR 7249, Aix-Marseille Université, Marseille, France.

[b] School of Mathematical and Physical Sciences, The University of Newcastle, Newcastle, Australia.

[c] CUDOS ARC Centre of Excellence, School of Physics, University of Sydney, Sydney, Australia.

[d] School of Mathematical Sciences, University of Technology, Sydney, Australia.

Published online: 27 Aug 2014.

To cite this article: Michael J.A. Smith, Michael H. Meylan, Ross C. McPhedran & Chris G. Poulton (2014): A short remark on the band structure of free-edge platonic crystals, Waves in Random and Complex Media, DOI: 10.1080/17455030.2014.936534

To link to this article: http://dx.doi.org/10.1080/17455030.2014.936534

Waves in Random and Complex Media, 2014
http://dx.doi.org/10.1080/17455030.2014.936534

Taylor & Francis
Taylor & Francis Group

A short remark on the band structure of free-edge platonic crystals

Michael J.A. Smith[a]*, Michael H. Meylan[b], Ross C. McPhedran[c] and Chris G. Poulton[d]

[a]*Institut Fresnel, UMR 7249, Aix-Marseille Université, Marseille, France;* [b]*School of Mathematical and Physical Sciences, The University of Newcastle, Newcastle, Australia;* [c]*CUDOS ARC Centre of Excellence, School of Physics, University of Sydney, Sydney, Australia;* [d]*School of Mathematical Sciences, University of Technology, Sydney, Australia*

(*Received 29 April 2014; accepted 15 June 2014*)

A corrected version of the multipole solution for a thin plate perforated in a doubly periodic fashion is presented. It is assumed that free-edge boundary conditions are imposed at the edge of each cylindrical inclusion. The solution procedure given here exploits a well-known property of Bessel functions to obtain the solution directly, in contrast to the existing incorrect derivation. A series of band diagrams and an updated table of values are given for the resulting system (correcting known publications on the topic), which shows a spectral band at low frequency for the free-edge problem. This is in contrast to clamped-edge boundary conditions for the same biharmonic plate problem, which features a low-frequency band gap. The numerical solution procedure outlined here is also simplified relative to earlier publications, and exploits the spectral properties of complex-valued matrices to determine the band structure of the structured plate.

1. Introduction

This paper presents a solution to the problem of a thin plate which is periodically perforated in two dimensions. The geometry of the inclusions is assumed to be circular, and consequently a solution using multipole methods can be obtained. For our purposes, it is assumed that free-edge boundary conditions are imposed at the edge of each inclusion. Multipole procedures have been used previously to obtain a general solution to a doubly periodic array of both clamped- and free- edge cylinders in thin plates,[1] as well as for the vanishing radius problem (i.e. the problem of a pinned plate).[1,2] The seminal paper by [1] provided numerical results in the form of band diagrams for all of these instances. However, the band diagrams presented in [1] for inclusions of finite radius were computed to dipolar order and were later found not to be fully converged. This was the primary motivation behind the follow-up work of [3], which provided fully converged values for the same systems of equations. Additionally, these expressions were also stated for completeness in (2.3.28a)–(2.3.28b) and (2.4.12a)–(2.4.12b) in [4]. Unfortunately, the system of equations used in all of these works is incorrect.

In particular, the expressions (5.4)–(5.5) in [1] (and subsequently used without derivation in later works) corresponding to the free-edge problem are wrong. In [1] they simplify their

*Corresponding author. Email: mike.smith@fresnel.fr

boundary condition expressions by taking a derivative of Bessel's equation (given in (3.7)–(3.8) of [1]). We believe that when they extended (3.8) to K_n, they failed to account for the sign change in the derivative compared to I_n. The derivation presented here does not rely on such complicated expressions and re-expresses the boundary conditions in a form which enables a solution in a fewer number of steps.

The authors believe it is important to provide this correction to both avoid confusion, and to inspire further theoretical and experimental investigation (as free-edge platonic crystals are the easiest to fabricate). The first experimental investigation into platonic cloaking was performed recently by [5]; however the authors are unaware of experimental research into periodically perforated plates. We believe that a straightforward experiment could easily be performed to validate the theory presented here by periodically drilling circular holes in a large, thin plate. One could then position a loudspeaker (or series of speakers) on one edge, and to prevent internal reflection from the other sides, damping materials/compounds could be used. From this design, one should be able to observe the lensing effects of platonic crystals for flexural waves, analogous to their photonic crystal counterparts.

Note that the solution procedure and table of values for *clamped-edge* boundary conditions in [1,3] have been independently validated by some of the authors using boundary integral methods,[4,6] and accordingly we are highly confident that the clamped-edge system and numerical results are correct for all of these papers.

Using this corrected system we are able to confirm that the free-edge problem has a spectral band at zero frequency, as we approach the center of the Brillouin zone, and compute these bands to high accuracy. This low-frequency feature of free-edge platonic crystals is analogous to the Neumann problem for a lattice of cylinders under the Helmholtz operator (or the two-phase problem, assuming source neutrality [7]), and also contrasts against the clamped-edge lattice problem for platonics which possesses a low-frequency band gap.[1]

2. Problem formulation

We begin with the frequency domain form of the biharmonic plate equation

$$(\Delta^2 - k^4)w(x, y) = (\Delta + k^2)(\Delta - k^2)w(x, y) = 0, \tag{1}$$

where $\Delta = \partial_x^2 + \partial_y^2$ denotes the two-dimensional Laplacian, $k^2 = \omega\sqrt{\rho h/D}$ is the nondimensionalized wave number and $w(x, y)$ denotes the displacement. Here D is the flexural rigidity, ρ is the mass density and h denotes the thickness of the plate.[1] Furthermore, we have assumed a time dependence of $\exp\{-\mathrm{i}\omega t\}$ where ω denotes the angular frequency.

The linearity of the biharmonic plate equation (1) admits a solution which is a superposition of the solutions to the Helmholtz and modified Helmholtz equations. This takes the form

$$w(x, y) = \sum_{n=-\infty}^{\infty} \Big[A_n J_n(kr) + E_n H_n^{(1)}(kr) + B_n I_n(kr) + F_n K_n(kr)\Big] \mathrm{e}^{\mathrm{i}n\theta}, \tag{2}$$

where (r, θ) denotes polar coordinates. We then impose free-edge boundary conditions for a circular inclusion of radius a, which are given correctly in [1,8] as:

$$\left\{\partial_r^2 w + \nu\left(\frac{1}{r}\partial_r w + \frac{1}{r^2}\partial_\theta^2 w\right)\right\}\Big|_{r=a} = 0, \tag{3a}$$

$$\left\{\partial_r^3 w + \frac{1}{r}\partial_r^2 w - \frac{1}{r^2}\partial_r w + \frac{2-\nu}{r^2}\partial_r\partial_\theta^2 w - \frac{3-\nu}{r^3}\partial_\theta^2 w\right\}\Big|_{r=a} = 0, \tag{3b}$$

where ν denotes the Poisson's ratio of the plate. These equations correspond to vanishing bending moment and shearing stress at the edges of the inclusion, and can be expressed in a more amenable form by noting that the Laplacian has the representation

$$\Delta w = \partial_r^2 w + \frac{1}{r}\partial_r w + \frac{1}{r^2}\partial_\theta^2 w, \tag{4}$$

and consequently, we can express (3a)–(3b) in the form

$$\Delta w\Big|_{r=a} = (1-\nu)\left(\frac{1}{r}\partial_r w + \frac{1}{r^2}\partial_\theta^2 w\right)\Big|_{r=a}, \tag{5a}$$

$$\partial_r(\Delta w)\Big|_{r=a} = (1-\nu)\left(\frac{1}{r^3}\partial_\theta^2 w - \frac{1}{r^2}\partial_r\partial_\theta^2 w\right)\Big|_{r=a}. \tag{5b}$$

Imposing the boundary conditions (5a) and (5b), where we observe that the Bessel functions given in (2) also satisfy the relations

$$\Delta\left(J_n(kr)e^{in\theta}\right) = -k^2 J_n(kr)e^{in\theta}, \tag{6a}$$

$$\Delta\left(H_n^{(1)}(kr)e^{in\theta}\right) = -k^2 H_n^{(1)}(kr)e^{in\theta}, \tag{6b}$$

and

$$\Delta\left(I_n(kr)e^{in\theta}\right) = k^2 I_n(kr)e^{in\theta}, \tag{6c}$$

$$\Delta\left(K_n(kr)e^{in\theta}\right) = k^2 K_n(kr)e^{in\theta}, \tag{6d}$$

one obtains the system

$$A_n\xi^+(J_n) + E_n\xi^+(H_n^{(1)}) + B_n\xi^-(I_n) + F_n\xi^-(K_n) = 0, \tag{7a}$$

$$A_n\eta^+(J_n) + E_n\eta^+(H_n^{(1)}) + B_n\eta^-(I_n) + F_n\eta^-(K_n) = 0, \tag{7b}$$

where for compactness we have defined the functions

$$\xi^\pm(\zeta_n) = (1-\nu)a\zeta_n'(ka) - n^2(1-\nu)\zeta_n(ka) \pm a^2k^2\zeta_n(ka), \tag{8a}$$

$$\eta^\pm(\zeta_n) = \pm k^2a^3\zeta_n'(ka) - n^2(1-\nu)\left[\zeta_n(ka) - a\zeta_n'(ka)\right]. \tag{8b}$$

Here ζ_n denotes an arbitrary Bessel function with the derivative defined as:

$$\zeta_n'(ka) = \frac{\partial}{\partial r}\zeta_n(kr)\Big|_{r=a}.$$

The definition of the derivative above differs from [1,3], but is chosen as this form results in fewer terms present in the system above. We include definitions of the derivatives in Appendix 2. To obtain our final system, we then use Rayleigh identities, which relate the regular component of the field near the nth scatterer to the corresponding scattered fields

generated by all other cylinders in the array.[9] These are given by [1,7]

$$A_n = \sum_{m=-\infty}^{\infty} (-1)^{n+m} S^{\mathrm{H,A}}_{m-n}(k, \boldsymbol{\kappa}) E_m, \tag{9a}$$

$$B_n = \sum_{m=-\infty}^{\infty} (-1)^{m} S^{\mathrm{K,A}}_{m-n}(k, \boldsymbol{\kappa}) F_m, \tag{9b}$$

where $\boldsymbol{\kappa}$ denotes the Bloch vector, which gives

$$\left[\sum_{m=-\infty}^{\infty} (-1)^{n+m} S^{\mathrm{H,A}}_{m-n} E_m\right] \xi^{+}(J_n) + E_n \xi^{+}(H_n^{(1)}) + \left[\sum_{m=-\infty}^{\infty} (-1)^{m} S^{\mathrm{K,A}}_{m-n} F_m\right] \xi^{-}(I_n) + F_n \xi^{-}(K_n) = 0, \tag{10a}$$

and

$$\left[\sum_{m=-\infty}^{\infty} (-1)^{n+m} S^{\mathrm{H,A}}_{m-n} E_m\right] \eta^{+}(J_n) + E_n \eta^{+}(H_n^{(1)}) + \left[\sum_{m=-\infty}^{\infty} (-1)^{m} S^{\mathrm{K,A}}_{m-n} F_m\right] \eta^{-}(I_n) + F_n \eta^{-}(K_n) = 0. \tag{10b}$$

The key difference between our system and the one given in [1,3] is that our Equations (7b) and (10b) do not feature a $(3 - \nu)$ term. To obtain a numerical solution, the m and n indices can be truncated and the subsequent system can be represented in the block matrix form

$$\left[\begin{array}{c|c} \mathbf{A}_{11} & \mathbf{A}_{12} \\ \hline \mathbf{A}_{21} & \mathbf{A}_{22} \end{array}\right] \left[\begin{array}{c} \mathbf{E} \\ \hline \mathbf{F} \end{array}\right] = \left[\begin{array}{c} \mathbf{0} \\ \hline \mathbf{0} \end{array}\right], \tag{11}$$

where representations for the lattice sums $S^{\mathrm{H,A}}_m$ and $S^{\mathrm{K,A}}_m$ can be found in Appendix 1.

3. Numerical solution

In this section, we will provide an updated series of images corresponding to those presented in [1,3]. That is, from the block matrix system $\mathbf{Ag} = \mathbf{0}$ in (11) where $\mathbf{A} = \mathbf{A}(k, \boldsymbol{\kappa}, \nu, a)$, we fix the Bloch vector $\boldsymbol{\kappa}$ and search through k space for $\det(\mathbf{A}) = 0$. These k values form continuous curves in Fourier space and are collectively referred to as the band structure of a crystal. This band structure can be compactly represented by parametrizing the edge of the irreducible Brillouin zone to generate a band diagram which reveals, among other things, regions of k space corresponding to complete reflection of energy (band gaps). An outline of the Brillouin zone and irreducible Brillouin zone is given in Figure 1.

In practice however, it is much more numerically stable to use the minimum eigenvalue ($\min\{\sigma_j\}$) of $\mathbf{A}$ as a proxy for vanishing determinant. This avoids the inherent instability of the matrix $\mathbf{A}$ which has large off-diagonal terms courtesy of the lattice sums, and can give rise to a poorly invertible (and thus ill-conditioned) matrix at values which do not correspond to band surfaces. Alternatively, Antipov normalization [7] could be used to

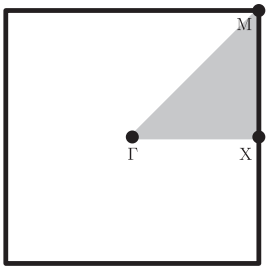

Figure 1. An outline of the Brillouin zone in $\boldsymbol{\kappa}$ space, with the irreducible Brillouin zone shaded. The symmetry points Γ, X and M are also shown, corresponding to $\boldsymbol{\kappa} = (0, 0)$, $\boldsymbol{\kappa} = (\pi/d, 0)$ and $\boldsymbol{\kappa} = (\pi/d, \pi/d)$, respectively.

rescale each block matrix term to a leading diagonal matrix, however the procedure used here works suitably well for our purposes.

In contrast to the pinned or clamped-edge array problem, where light lines correspond to the singularities of the lattice sum $S_m^{\mathrm{H,A}}$, the location of the light lines for the free-edge problem are shifted in k-space by the boundary operators ξ^+ and η^+, as is observed in the system (10a)–(10b). We can distinguish between these light lines and actual roots by observing the minimum singular value of $\mathbf{A}$.

Using the method described above, one can compute the band structure of the crystal for some arbitrary truncation M. We demonstrate the efficacy of the solution method here in Figure 2 at $\boldsymbol{\kappa} = (\pi/(2d), 0)$ for a circular inclusion of radius $a = 0.35$ with $d = 1$ and $\nu = 0.3$, corresponding to a truncation of $M = 3$. Here we observe zeros at $k = 1.4363$, $k = 4.4271$, $k = 6.0837$, $k = 6.4709$, $k = 7.6750$, $k = 7.9164$ and $k = 9.3327$. Also shown is the minimum singular value of $\mathbf{A}$ (broken red line) which takes minimum values at the actual zeros, in contrast to the shifted light lines which feature throughout. These shifted light lines can be observed as sharp vertical transitions in $\min\{\sigma_j\}$. Note that the fully converged values for these zeros are given in Table 1, and the corresponding band diagram for $a = 0.35$ is given in Figure 4.

In Figure 3, we provide the band diagram corresponding to radius $a = 0.2$ for a square array of period unity. This band diagram features a series of band crossings, a Dirac point at $k(\Gamma) = 6.0244$ and two-fold degeneracies at $k(\Gamma) = 8.6018$ and $k(\mathrm{X}) = 6.8580$. Within the interval $0 < k < 9$, there are no complete band gaps. Qualitatively this diagram is similar to Figure (2a) presented in [3]. We include the band diagrams for both k and k^2 here as both measures are used in [1,3]. However, given that $\omega \propto k^2$, we feel that the quadratic form should be used as standard convention for platonic crystals.

In Figure 4, we provide the band diagram corresponding to radius $a = 0.35$. Some interesting features include a Dirac point at $k(\mathrm{M}) = 3.9440$ and a double degeneracy at $k(\Gamma) = 5.8192$, in addition to a series of band crossings. This image bears a vague similarity to Figure (2b) in [3] but ultimately demonstrates a linear acoustic band in k and fully converged band curves for the correct system. As in Figure 3, band diagrams for both k and k^2 are presented.

The fundamental mode of vibration corresponding to $\boldsymbol{\kappa} = (\pi/(2d), 0)$ for $a = 0.2$ and $\nu = 0.3$ is presented in Figure 5, over the Wigner–Seitz cell (WSC). An associated contour plot is given in Figure 6. This is an updated image to Figures (6a) and (6b) given in [1] and

Table 1. Converged values for k for a square array ($d = 1$) corresponding to various radii a under free-edge boundary conditions. These values are calculated at the midpoint of each line segment along the edges of the IBZ. Also shown are the numbers of multipoles required for convergence to 6dp.

a	0.1		0.15		0.2		0.25		0.3		0.35		0.4	
ΓX	1.556041	4	1.539375	4	1.518097	5	1.493135	5	1.465175	7	1.434339	7	1.398260	9
	4.678641	4	4.646675	5	4.600759	6	4.540085	6	4.475129	7	4.420142	8	4.389344	10
	6.434087	5	6.341440	5	6.202691	5	6.085016	7	6.034019	7	6.042066	9	6.053526	10
	6.437154	5	6.452677	4	6.496404	6	6.525940	5	6.510606	8	6.454963	8	6.389674	9
	7.779945	5	7.662352	4	7.542944	6	7.479681	7	7.477269	7	7.641905	7	7.910918	9
	7.785910	5	7.669497	6	7.556259	7	7.511610	6	7.587437	8	7.743473	7	8.126660	9
XM	3.475146	4	3.453937	4	3.400427	4	3.315702	4	3.212228	6	3.100997	7	2.991126	12
	3.493169	4	3.459395	4	3.444270	5	3.444061	5	3.445225	6	3.438894	8	3.417056	11
	5.625550	4	5.569118	4	5.484814	5	5.383375	5	5.273966	6	5.158805	8	5.038946	11
	5.625985	4	5.611772	5	5.613454	5	5.670795	6	5.858507	6	6.270635	8	7.034158	10
	8.393816	4	8.337022	5	8.291084	6	8.207405	7	8.100605	8	7.971978	9	7.835569	15
	8.423253	5	8.365497	6	8.325599	6	8.385595	7	8.497142	6	8.705147	9	8.961322	10
MΓ	2.201633	5	2.180700	4	2.154955	4	2.124813	5	2.089823	6	2.048935	6	1.998641	11
	4.929620	4	4.873939	5	4.773347	6	4.649038	6	4.525583	7	4.423025	8	4.356613	12
	4.935147	4	4.927477	5	4.949167	5	4.989004	6	5.037270	6	5.069941	8	5.055983	13
	6.622465	5	6.575910	5	6.509827	6	6.473665	7	6.543070	7	6.816032	8	7.421559	11
	7.948975	4	7.853432	5	7.737277	6	7.638112	6	7.559662	8	7.492670	9	7.424720	11
	7.974427	5	7.980388	6	8.055490	6	8.180480	6	8.277725	7	8.343457	9	8.406089	13

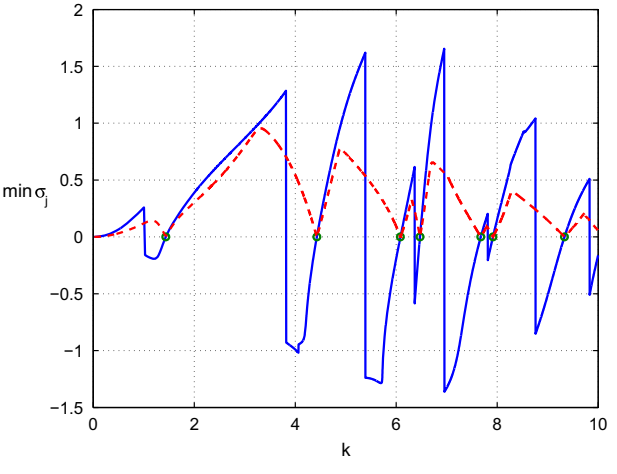

Figure 2. Plot of the minimum eigenvalue σ of $\mathbf{A}$ for $\boldsymbol{\kappa} = (\pi/(2d), 0)$ (blue) and minimum singular value (broken red) for $a = 0.35$, $d = 1$, and $\nu = 0.3$. Genuine roots of the dispersion relation are highlighted with green dots. A truncation of $M = 3$ is considered here for illustrative purposes.

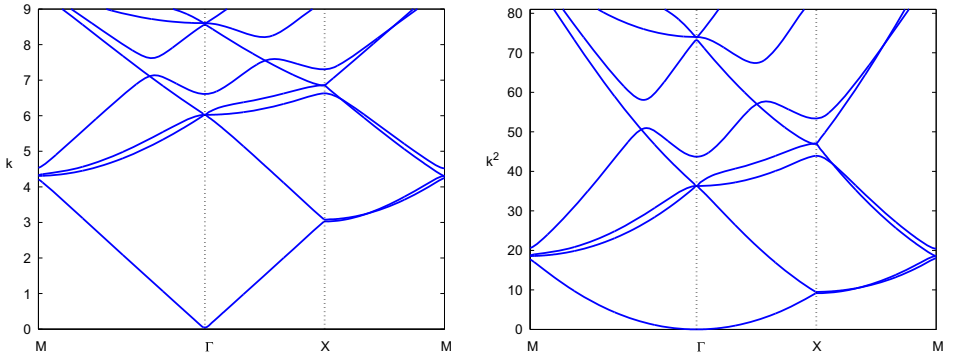

Figure 3. Converged band diagrams for a square array of period $d = 1$ for $a = 0.20$ and $\nu = 0.3$ ($M = 8$).

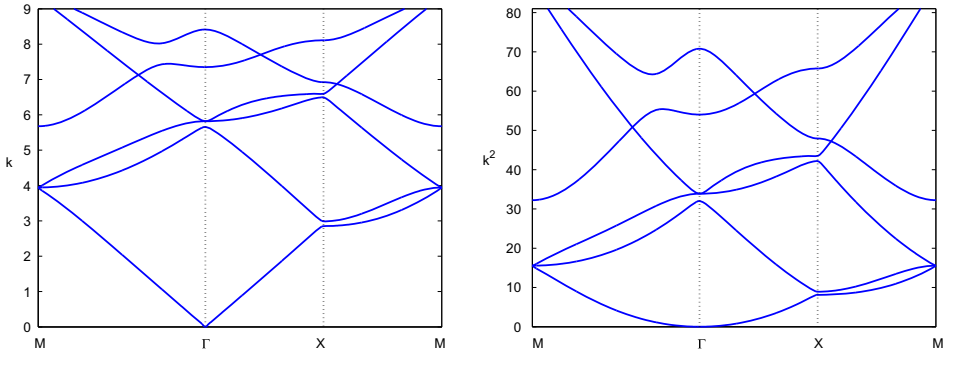

Figure 4. Converged band diagrams for a square array of period $d = 1$ for $a = 0.35$ and $\nu = 0.3$ ($M = 10$).

bears some resemblance to the figures presented there. Note that the mode given here has been scaled such that $\int_{WSC} |w|^2 \mathrm{d}x\mathrm{d}y = 1$.

In Table 1, we present the first six k values at select points in the Brillouin zone corresponding to a range of cylinder radii a. Note that for this table, we use the high-precision algorithm outlined in [10], using the minimum eigenvalue (at low truncation) as an initial value for the method, and then searching for $\det(\mathbf{A}) = 0$ in the immediate neighborhood of that point. The truncation M is then increased and the procedure repeated until the value is stable at the sixth decimal place. This varies from the table presented in [3] which provides accuracy to within 0.1%. We revert back to the determinant for this algorithm because the surface formed by the minimum eigenvalue is not necessarily an analytic function in complex space, in contrast to the full determinant or the minimum singular value of $\mathbf{A}$. We compute values at the midpoint of each edge of the irreducible Brillouin zone (i.e. $\boldsymbol{\kappa} = (\pi/(2d), 0)$ $\boldsymbol{\kappa} = (\pi/d, \pi/(2d))$, and $\boldsymbol{\kappa} = (\pi/(2d), \pi/(2d))$) and not at the symmetry points Γ, X and M. We find that for the free-edge problem compared to the clamped-edge problem, a larger level of truncation M is required for convergence.

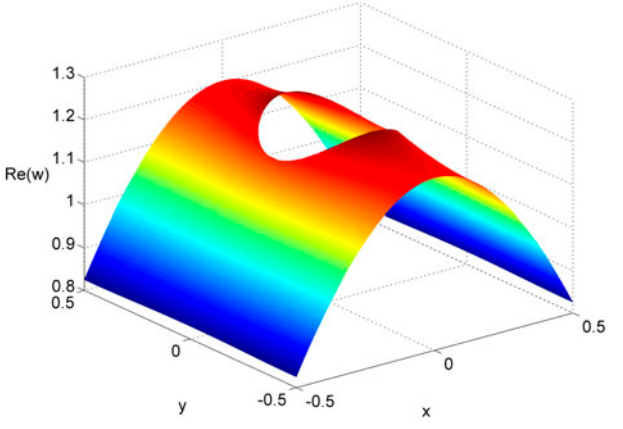

Figure 5. The fundamental mode of vibration over the fundamental cell at $k = 1.518097$ for $\boldsymbol{\kappa} = (\pi/(2d), 0)$, $a = 0.20$, $\nu = 0.3$ and $M = 5$, corresponding to a square array of period $d = 1$.

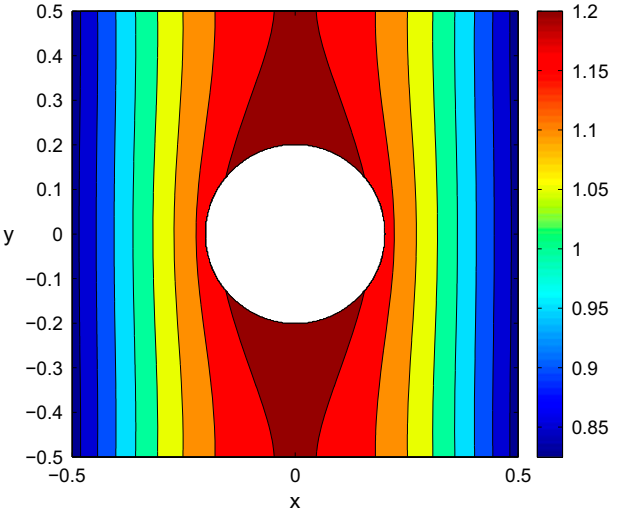

Figure 6. A contour plot of the fundamental mode corresponding to Figure 5.

However, as can be observed from Figure 2, we find that a truncation of $M = 3$ provides band diagram pictures that are qualitatively similar to the fully converged problem.

4. Concluding remarks

In this paper, we have investigated the propagation of Bloch–Floquet waves through periodically perforated plates, assuming free-edge conditions. In particular, we have presented a correction to the system originally given in [1] for this problem. Corrected tables and figures have also been presented from the known publications on this topic. In

light of our figures and table, it appears that the error presents itself significantly at larger radius a. Present work by some of the authors suggests that this error has more of an effect for the corresponding one-dimensional array problem, which replaces the lattice sums with grating sums and features a forcing. An interesting next step in theoretical platonics would be an investigation of the asymptotics for the lowest spectral band observed here.

References

[1] Movchan AB, Movchan NV, McPhedran RC. Bloch–Floquet bending waves in perforated thin plates. Proc. R. Soc. A: Math. Phys. Eng. Sci. 2007;463:2505–2518.

[2] Smith MJA, McPhedran RC, Poulton CG, Meylan MH. Negative refraction and dispersion phenomena in platonic clusters. Waves Random Complex. 2012;22:435–458.

[3] Poulton CG, McPhedran RC, Movchan NV, Movchan AB. Convergence properties and flat bands in platonic crystal band structures using the multipole formulation. Waves Random Complex. 2010;20:702–716.

[4] Smith MJA. Wave propagation through periodic structures in thin plates [dissertation]. Auckland: The University of Auckland; 2013.

[5] Stenger N, Wilhelm M, Wegener M. Experiments on elastic cloaking in thin plates. Phys. Rev. Lett. 2012;108:014301.

[6] Smith MJA, Meylan MH, McPhedran RC. Flexural wave filtering and platonic polarizers in thin elastic plates. Q. J. Mech. Appl. Math. 2013;66:437–463.

[7] Movchan AB, Movchan NV, Poulton CG. Asymptotic models of fields in dilute and densely packed composites. London: Imperial College Press; 2002.

[8] Leissa AW. Vibration of plates. Washington (DC): NASA SP-160; 1969.

[9] Botten LC, McPhedran RC, Nicorovici NA, Asatryan AA, de Sterke CM, Robinson PA, Busch K, Smith GH, Langtry TN. Rayleigh multipole methods for photonic crystal calculations. Prog. Electromagn. Res. 2003;41:21–60.

[10] Meylan MH, Gross L. A parallel algorithm to find the zeros of a complex analytic function. ANZIAM J. 2008;44:236–254.

[11] Abramowitz M, Stegun IA. Handbook of mathematical functions with formulas, graphs, and mathematical tables. New York (NY): Dover; 1972.

Appendix 1. Accelerated lattice sums

The accelerated expressions for the lattice sums presented in the Rayleigh identities (9a) and (9b) can be found in [1] and are included here for completeness. For the case of a square array of period d, they are given by

$$S_m^Y(k,\boldsymbol{\kappa}) = \frac{1}{J_{m+3}(k\lambda)}\left(-\left[Y_3(k\lambda)+\frac{1}{\pi}\sum_{n=1}^{3}\frac{(3-n)!}{(n-1)!}\left(\frac{2}{k\lambda}\right)^{3-2n+2}\right]\delta_{m,0}\right.$$
$$\left.-\frac{4\mathrm{i}^m}{d^2}\sum_p\left(\frac{k}{Q_p}\right)^3\frac{J_{m+3}(Q_p\,\lambda)}{Q_p^2-k^2}\mathrm{e}^{\mathrm{i}m\theta_p}\right), \tag{A1a}$$

and

$$S_m^K(k,\boldsymbol{\kappa}) = \frac{1}{I_{m+3}(k\lambda)}\left(\left[K_3(k\lambda)-\frac{8}{(k\lambda)^3}+\frac{1}{k\lambda}-\frac{k\lambda}{8}\right]\delta_{m,0}\right.$$
$$\left.+\frac{2\pi\mathrm{i}^m}{d^2}\sum_p\left(\frac{k}{Q_p}\right)^3\frac{J_{m+3}(Q_p\,\lambda)}{Q_p^2+k^2}\mathrm{e}^{\mathrm{i}m\theta_p}\right), \tag{A1b}$$

where δ_{mn} is the Kronecker delta, $\theta_p = \arg \mathbf{Q}_p$, $\mathbf{Q}_p = (\kappa_x + 2\pi h_1/d, \kappa_y + 2\pi h_2/d)$, $Q_p = \|\mathbf{Q}_p\|_2$, and the vector $\boldsymbol{\lambda}$, with corresponding norm λ, represents an arbitrary vector positioned inside the first Brillouin zone. Here we have used an acceleration parameter of 3, and $h_1, h_2 \in \mathbb{Z}$.

Appendix 2. Derivatives of Bessel functions

The recurrence relations for derivatives of Bessel functions can be found in (9.1.27) and (9.6.26) of [11], and we include these here both for completeness and to emphasize the sign changes in the derivatives of modified Bessel functions. In our notation, these admit the following expressions

$$J_n'(ka) = \frac{\partial}{\partial r} J_n(kr)\big|_{r=a} = \frac{k}{2}\left[J_{n-1}(ka) - J_{n+1}(ka)\right], \tag{A2a}$$

$$H_n^{(1)\prime}(ka) = \frac{\partial}{\partial r} H_n^{(1)}(kr)\big|_{r=a} = \frac{k}{2}\left[H_{n-1}^{(1)}(ka) - H_{n+1}^{(1)}(ka)\right], \tag{A2b}$$

and

$$I_n'(ka) = \frac{\partial}{\partial r} I_n(kr)\big|_{r=a} = \frac{k}{2}\left[I_{n-1}(ka) + I_{n+1}(ka)\right], \tag{A2c}$$

$$K_n'(ka) = \frac{\partial}{\partial r} K_n(kr)\big|_{r=a} = -\frac{k}{2}\left[K_{n-1}(ka) + K_{n+1}(ka)\right]. \tag{A2d}$$